Release of contaminants from a heterogeneously fractured low permeability unit underlying a DNAPL source zone

Dearden, R.A.[1*], Noy, D.J. [1], Lelliott, M.R. [2], Wilson, R.[3] and Wealthall, G.P.[1]

[1]British Geological Survey, Keyworth, Nottinghamshire, NG12 5GG (*corresponding author: R. Dearden),

[2] RPS Group, 701 San Business Centre, 8th Khoroo, Sukhbaatar District, Ulaanbaatar, Mongolia

[3]Department of Civil and Structural Engineering, Kroto Research Institute, North Campus, University of Sheffield, Broad Lane, Sheffield, S3 7HQ

1 Introduction

Dense non-aqueous phase liquids (DNAPLs) are common groundwater contaminants that have historically been released from degreasing and dry cleaning industries (Doherty, 2000; Pankow and Cherry, 1996). DNAPLs are immiscible in water and exhibit a density greater than 1 g/cm^3; when released to the ground, the non-aqueous phase liquid (NAPL) migrates downwards under the influence of gravity following a path of least capillary resistance (Mercer and Cohen, 1990). The solubility of many DNAPLs can be several orders of magnitude over their regulatory limits and therefore DNAPL source zones can, and do, lead to extensive and persistent groundwater pollution (Mackay and Cherry, 1989).

Where low permeability sedimentary deposits (e.g. clay, till, mudstone and chalk) occur in the path of downward DNAPL migration, the small pore throat sizes and associated higher entry pressures usually result in pooling of DNAPL at the differential permeability interface (Feenstra et al., 1996). The mechanisms controlling further downward migration are dependent on the presence or absence of secondary

permeability features including fractures, dissolution features and coarse-grained interbeds. Where fractures are absent, inward migration is restricted to dissolved phase diffusion into the matrix (Johnson et al., 1989); a process which is driven by high inward concentration gradients created by DNAPL constituent aqueous-solubility concentrations at the interface (Figure 1a). Whilst concentrations immediately beneath the interface are likely to be near-solubility, these decrease rapidly with depth, for example Parker et al. (2004) observed a decline in concentration from that indicative of DNAPL presence (320 µg/g) to <30 µg/g (wet soil) over a distance of ~1 m through a clayey silt aquitard that was overlain by pooled NAPL residing in a sand aquifer. Conversely where fractures are present, inward DNAPL migration, controlled by the fracture aperture and associated capillary entry pressures (Kueper and McWhorter, 1991), result in the potential for DNAPL mass to enter and reside within the fractures. The dissolution of DNAPL constituents and subsequent diffusion of the dissolved phase from the fractures results in significant aqueous- and sorbed-phase mass within the matrix (Espositio and Thomson, 1999; Parker et al., 2008; Parker et al., 1994; Reynolds and Kueper, 2004; Sale et al., 2008). Through successive fracture replenishments by DNAPL, mass stored in the matrix can increase until the pore water concentration asymptotically reaches the contaminant solubility throughout the matrix (Parker et al., 1997).

Secondary contaminant sources are formed when concentrations within low permeability media exceed those in bounding higher permeability aquifers (Chapman and Parker, 2005; Liu and Ball, 2002; Mutch et al., 1993). The resulting reversed concentration gradients result in mass flux out of the low permeability sediments, which in the absence of fractures is limited to diffusive mass discharge across the

lithologic interface (Figure 1b). The presence of fractures greatly increases the surface area available for diffusive mass discharge from the matrix and decreases the diffusion path lengths (Parker et al., 1994). Per unit volume of media, more mass can diffuse into mobile pore space (the fractures) and therefore can cause greater, early-time impact to the overlying high permeability media. Upward gradients across low permeability media also add an advective component to upward mass transport, increasing overall mass discharge. This is particularly important in fractures, where increased flow leads to greater fracture dilution that maximises concentration gradients across the fracture walls. The importance of fracture aperture on fracture dilution and mass removal was demonstrated by Falta (2004) who simulated TCE DNAPL placement, dissolution and matrix diffusion in a fracture over a 20-year equilibration time. After this time, clean water flushing was simulated through the fracture. Fracture effluent concentrations in the 30 µm and 100 µm aperture fractures after a simulated 100 years of flushing were ~900 µg/l and ~90 µg/l respectively. For the same driving hydraulic head, the higher volumetric flux in the fractures with larger aperture removed more TCE mass per unit time, minimising fracture concentrations and therefore imposing higher concentration gradients and hence higher TCE removal rates from the matrix.

Efforts to address contaminants in low permeability zones have included use of pneumatic and hydraulic fracturing (Christiansen et al., 2008; Slack et al., 2000). These techniques aim to optimise fracture spacing and aperture to decrease matrix diffusion distances and provide porosity for the injection of remedial fluids (USEPA, 1994). Research has focused on the depletion of VOCs within fractures by oxidation or biodegradation for example (Chambon, 2010; Hønning et al., 2007); a process which aims to reduce concentrations within the low permeability deposit thereby

decreasing the outward mass flux. Whilst mechanically-induced fracturing provides an opportunity for remediation of mass in low permeability deposits, it may not be practical at all sites. Where it is practical, an understanding of mass flux from naturally fractured deposits is vital for predicting recontamination potential, such that a baseline mass flux can be estimated.

This paper reports on a fractured mudstone secondary source zone at an industrial site in the UK that was investigated as part of the SABRE (Source Area BioRemediation) project. The aim of this study was to determine the potential of a fractured sedimentary deposit to recontaminate an aquifer. We considered inward contaminant transport, the resultant contaminant distribution and the effects of site-scale variation in fracture spacing and aperture on outward mass flux. We report on the invasion of trichloroethene into mudstone and predict the likely inward transport processes. We show that remediation of the bounding aquifer led to a concentration gradient from the mudstone, which represented a secondary source zone of unknown magnitude and duration. Via numerical modelling, we investigated the importance of heterogeneity in concentration and fracture distribution on outward mass flux from the mudstone. In so doing, we test the hypothesis that it is necessary to characterise the fracture aperture and spacing within secondary source zones in order to accurately estimate the potential magnitude and duration of recontamination. Such understanding may prompt actions to enhance fracture aperture and spacing to accelerate mass removal, and/or design associated means to mitigate the resulting aquifer recontamination.

2 Field site

2.1 SABRE Industrial site

The site located within the United Kingdom in a wide, shallow valley on a river terrace, which locally forms a minor aquifer (Figure 2). The site was formerly occupied by a monochloroacetic acid (MCA) production facility that was operational between 1963 and 1990. TCE was stored on-site, used in industrial processes and subsequently disposed to a near-surface sump. Spillages occurred during this period resulting in a DNAPL source zone within the shallow river terrace aquifer. This source zone was the focus of the SABRE bioremediation study (Buss et al., 2010). As part of this study, the source zone was isolated by a three-sided, 30 m-long, 4 m-wide cell, constructed from plastic sheet piles that were keyed into the mudstone at ~7 m depth. Flow was induced into the cell from the upgradient open-end, by abstraction from two wells positioned at the downgradient closed-end. The source zone within the cell was treated using enhanced bioremediation, a process that involved a single addition of SRS™ (soya bean oil) and a microbial culture including *Dehalococcoides ethenogens* (KB-1™) to the subsurface. The sequential degradation of trichloroethene (TCE), to cis-1,2-dichloroethene (cDCE), vinyl chloride (VC) and ethene (Ee) was monitored over the 650-day experiment via a network of over 450 sample locations (monitoring wells and multilevel samplers).

The geology at the site comprised a sequence of alluvial clays, silts and sands (~2 m thick) overlying coarser sand and river terrace gravel deposits (~4 m thick). Red Triassic mudstone belonging to the Gunthorpe Formation (Mercia Mudstone Group) was present below these deposits (~50 m thick), beneath which the Sherwood Sandstone aquifer was present. Residual DNAPL was identified in cores from the

alluvium and river terrace gravel deposits. Natural groundwater flow in the shallow aquifer is principally horizontal within the terrace gravel deposits (hydraulic gradient: 0.001 – 0.002, hydraulic conductivity: 0.01 to 26 m/d); vertical hydraulic gradients are negligible.

The Triassic Mercia Mudstone is the focus of this study. It typically comprises interbedded, reddish-brown, orangish brown, and subordinate greyish green mudstone, siltstone and very fine grained sandstone with thin beds of gypsum or anhydrite (Hobbs et al., 2002). The formation was deposited under Sabkha desert conditions in hypersaline and evaporitic mudflat environments, resulting in thick sequences of mud, silt and fine sand, interspersed with thin beds and veins of halite and gypsum. A marine transgression in the late Triassic resulted in burial, which is now marked by an unconformity (Hobbs et al., 2002). At depth and in the presence of geothermal gradients, gypsum dehydrates to anhydrite (Aljubouri, 1971); then on exhumation, the reaction is reversed with the reformation of gypsum (Murray, 1964). Of key importance is the latter reaction, which occurs in the near-surface zone where groundwater is present, resulting in a 63% increase in mineral volume inducing fracturing and brecciation (Shearman et al., 1972). Further exposure to groundwater results in gypsum dissolution and thus open fractures, the hydraulic connectivity of which is demonstrated by: the occurrence of the flow which initiated the dissolution of gypsum (Seedhouse and Sanders, 1990; Wilson, 2003); chemical signatures of mudstone-derived minerals in the adjacent aquifer (Allen et al., 1997; Kimblin, 1995), and in a location 5 km from the industrial site, postglacial-age gypsum precipitation in the vadose zone (Jones, 1974). The mudstone matrix is characterised by low permeabilities with laboratory-derived values of 10^{-4} to 10^{-6} m/d perpendicular to

bedding. Field permeabilities meanwhile range from 10^{-1} to 10^{-3} m/d, mainly parallel to bedding, likely reflecting flow in fractures and more permeable horizontal beds (Tellam and Lloyd, 1981). These horizontal beds, known as skerries, comprise siltstone and fine-grained sandstone bands, which can yield 25-130 m^3/d (Jones et al., 2000). At the site, upward hydraulic gradients of 0.02 to 0.10 were calculated within the mudstone, based on piezometric surfaces in the Sherwood Sandstone Formation compared to that in the shallow gravels.

3 Methods

3.1 Industrial site field characterisation

The locations of cored boreholes drilled in the river terrace gravels and the mudstone were selected to characterize VOC distribution sufficiently to: i) position the test cell; ii) delineate probable DNAPL and plume zones; iii) guide the installation of monitoring devices, and iv) provide representative mudstone samples from the suspected DNAPL zone for this study without unduly disturbing the test cell. Four boreholes (SN104, SN116, SN117 and SN118) were positioned in the source zone where contamination concentrations were known to be high and DNAPL presence was established in earlier investigation (Figure 3). Boreholes were positioned outside the footprint of the SABRE cell. To observe conditions downgradient from the DNAPL source zone, one borehole (SN120) was located in the plume zone where DNAPL was unlikely to be present. Boreholes were drilled to at least 11 m below ground surface, providing mudstone core in excess of 4.5 m.

Two drilling techniques were used. SN104 was collected using a Terramec 1000 rotary drill rig with Geobore S core barrel and water flush. Due to poor core recovery

using this technique SN116, SN117, SN118, and SN120 were collected using a rotary sonic drill rig. Core was recovered in 1.5 m long, 100 mm diameter clear plastic liners. Given that the DNAPL was present for between 15 and 37 years before coring commenced, remobilisation of DNAPL, as a result of drilling, was assumed to be unlikely within the gravels. This assumption is based on numerical modelling by Gerhard et. al. (2006) that determined time periods of months to a few years for cessation of mobilisation within deposits (sands) of similar hydraulic conductivities, but more importantly, the absence of DNAPL accumulations at the base of gravels within the core, observed previously by Parker et al., (2003).

Sub-samples were taken for TCE analysis within the lower 0.1-0.3 m of the terrace gravels to the base of the core at around 3-4 m below the mudstone interface. Samples were taken at 5 cm intervals in the upper 2 m of the core and at 10 cm in the remaining core. To minimise volatile losses, samples were recovered through holes (10-30 mm diameter) drilled through the core liner, using a stainless steel coring device (Parker et al., 2004). The core samples were analysed for volatile organic compounds (VOC), principally TCE, via a methanol extraction procedure as per USEPA method 5021A (USEPA, 2003). Samples were stored for two weeks prior to analysis, during which they were shaken using a vortex mixer to disaggregate solids and enhance the extraction of TCE into the methanol. Samples were fully disaggregated prior to analysis. Methanol sample aliquots were analysed via headspace using a Perkin Elmer Clarus 500 gas chromatograph with an Electron Capture Detector (ECD) under the following operating conditions: column, 30 m long, 530 μm dia., 3 μm of film fused silica; carrier gas, nitrogen; flow rate, 30 ml min^{-1}; injector temperature, 220 ºC; split ratio, 13.3:1; split flow, 50 ml min^{-1}; oven

temperature, 40 ºC for 10 mins, ramped to 190 ºC over 10 minutes, hold for 2 mins, ramped to 250 ºC over 30 mins; ECD detector temperature, 375 ºC. Data integration and control was performed using TotalChrom Client. Calibration was performed via the method described above, with the addition of methanol-based standards to headspace vials, rather than methanol sample aliquots. The calibration for TCE was linear (R^2 >99 %). The detection limit was 0.01 mg/kg. Dye tests for the direct determination of DNAPL were run on samples taken adjacent to the VOC sample depths. The hydrophobic dye tests using Sudan IV were implemented as per Parker et al., (2004). When added to samples containing DNAPL, Sudan IV powder partitions into the DNAPL producing a characteristic red colouration. Eighteen sub-samples were collected from three of the mudstone cores for microbiological characterisation and quantification of *Dehalococcoides spp* (Maymo-Gatell et al., 1997), the presence of which indicates potential for sequential biodegradation of TCE to cDCE, VC and ultimately to Ee, within the mudstone. Core subsamples were collected in sterile 50 ml centrifuge tubes and shipped at 4 ºC. Samples were analysed by SiREM (Guelph, Ontario) using Gene-Trac® VC tests that target the *Dehalococcoides* gene, vinyl chloride reductase (vcrA), which codes for the enzyme that dechlorinates vinyl chloride to ethene (Scheutz et al., 2008).

A partitioning calculation as shown in Equation 1 (Feenstra et al., 1991) was used to determine the phase of TCE present in solid samples:

$$C_w = \frac{C_s \rho_b}{K_d \rho_b + \emptyset_w}$$

Equation 1

where C_w is pore water concentration, C_s is total soil concentration, ρ_b is bulk density, K_d is partitioning coefficient (calculated via $K_d = f_{oc} * K_{oc}$) and $\emptyset_w$ is water-filled

porosity. By assuming that the pore waters in a core sample are saturated with TCE (i.e. C_w =1100 mg/L), the equation can be rearranged to yield the soil concentration above which DNAPL must be present. This value is termed the DNAPL threshold and values of 622 mg/kg and 410 mg/kg were calculated for the river terrace gravels (C_w; 1100 mg/l, ρ_b; 2.0 g/cm^3, K_{oc}; 113 l/kg, f_{oc}; 0.005, $\varnothing_w$; 0.3) and mudstone (C_w; 1100 mg/l, ρ_b; 1.68 g/cm^3, K_{oc};113 l/kg, f_{oc}; 0.002, $\varnothing_w$; 0.29) respectively. Bulk density values were obtained gravimetrically. Porosity was calculated via $\varnothing_w = V_w / (V_s + V_w)$, where V_w is volume of water and $V_s = m_s/\rho_p$, where V_s is volume of solid; m_s is mass of solid and ρ_p is particle density. The partitioning coefficient, K_d was calculated via $f_{oc} * K_{oc}$, where f_{oc} was determined using a total organic carbon analyser (Scientifics, UK) and K_{oc} was determined via $\log K_{oc} = a \log K_{ow} + b$, where a is 0.827, b is -0.039 and $\log K_{ow}$ is 2.53 ml/g (Cohen et al., 1993; Pankow and Cherry, 1996). It is acknowledged that sorption of TCE (up to 2000 µg/l) to clayey deposits is likely to be underestimated by the $f_{oc} * K_{oc}$ relationship at low concentrations (Allen-King et al., 1997) potentially resulting in a higher DNAPL threshold, however in this case, a sensitivity analysis showed that the resulting variation was likely to be insignificant. Partitioning calculations were also used to determine respective pore water concentrations from total concentrations found in sediment samples. The equation does not explicitly account for TCE in the DNAPL-phase and therefore when applied to samples containing DNAPL, the pore water concentration was calculated to be greater than TCE solubility. In such cases, the pore water concentration was assigned a value of TCE solubility and the remaining mass was assumed to be present as a NAPL phase.

3.2 Analog site field methods

It was not possible to directly observe the nature of the mudstone surface at the experimental site. Potential geochemical and hydrological disturbance to the SABRE

experiment, also prevented hydraulic testing of the mudstone. Therefore, the nearest location where the mudstone was exposed was selected for measurement of in-situ mudstone fractures. The analog site was an uncontaminated quarry site located roughly 10 km from the experimental site in the same wide, shallow river valley. The quarry had been dewatered to allow removal of the river terrace sand and gravel, resulting in the exposure of the underlying mudstone. An area of 12 m^2, surrounded on two sides by 1.5 m deep drainage ditches, was cleared of sand and gravel to expose the mudstone surface immediately prior to fracture mapping. The area was divided into 1 m squares and fractures present both on the mudstone surface and within the drainage ditch walls were mapped. In the drainage ditch wall, preferential flow features which intersected the line of the tape measure (termed the scanline) were recorded. Fracture apertures (denoted by *2b*) less than 1 mm were measured using feeler gauges, whilst apertures over 1 mm were measured using a ruler. The smallest aperture values recorded along the ditch scanline were 0.01 mm, likely reflecting the visual detection limit. All measured apertures represent estimates of physical rather than hydraulic apertures. Apertures may vary with depth. Fracture spacing measurements were recorded along the scanline. On the mudstone surface, fracture apertures that were visible (>1 mm) were measured every 10 cm along the fracture trace. Fracture spacings were measured between each fracture every 0.5 m. Fracture sediment fills were noted where present.

3.3 Numerical modelling approach

The 2-D, Laplace Transform Galerkin (LTG), finite element model, Fractran (Sudicky and McLaren, 1992) was used to simulate back diffusion of TCE after remediation of the overlying aquifer. The model domain, shown schematically in Figure 4, comprised a vertical section 4 m (81 nodes) wide and 5 m (101 nodes) deep. This spatial

discretization may appear relatively coarse, however is appropriate and yields highly accurate solutions because calculations are smoother within the Laplace domain than in the conventional time domain (Sudicky, 1989; Sudicky and McLaren, 1992). Fractran model outputs of concentration as a function of distance for a 5-year model run were almost identical to a one-dimensional analytical solution, verifying the chosen discretization.

Boundary conditions for the vertical sides were zero flux/zero gradient. The top and bottom boundaries were assigned specified head (site-specific vertical hydraulic gradients) and permitted TCE outward flux. Simulations assumed that mass emanating from the top of the domain was degraded or diluted to below detection limits rapidly and, hence the domain was truncated at the upper mudstone interface. The concentration in the overlying river terrace gravels was therefore assumed to be zero and hence representative of a well-flushed aquifer in which biodegradation, dilution and sorption were optimised. These processes were not simulated due to a lack of parameters to characterize that attenuation. This simplification should not compromise the overall results because the objective here is to examine the affects of varying fracture properties rather than to simulate site-specific concentrations. The vertical extent of the model domain was such that basal mass flux was negligible. The sensitivity of parameters was considered by reference to previous studies that illustrate the importance of fracture aperture and spacing (Mackay and Cherry, 1989; White, 2007). Site-specific fracture property values were unknown and hence two sets of values were used to predict outward mass flux: a) values typical of clays (Parker et al., 1994) and b) values observed at the analog site (Table 1). Both instantaneous and cumulative mass flux values were reported at the top horizontal boundary. The

mudstone matrix was modelled as homogeneous clay, which is assumed to be a reasonable representation of the extensively weathered and reworked upper 5 m of the mudstone. The initial concentration distribution within the mudstone domain was described by either: i) a homogenous concentration of 1 throughout the domain, or ii) vertical log-linear decay with a concentration of 1 at the upper boundary. Model results were therefore expressed as fractions of the maximum concentration. To deduce site-specific fluxes, the fractions were multiplied by the site maximum concentration of 1100 mg/l.

4 Results and Discussion

4.1 Contaminant invasion

Three of the four cores recovered within the DNAPL source zone recorded DNAPL in the river terrace gravels directly above the mudstone interface, indicating that DNAPL was in contact with the mudstone surface. Indeed, DNAPL was pumped from a multilevel port that terminated immediately above the mudstone surface (position shown by black cross in Figure 3). Residual saturation values within this zone ranged from 1.2% to 13.7% (assuming a porosity of 0.3). Given that spills may have occurred throughout the previous 27-45 years, it is possible that DNAPL may have been pooled at the interface for many years. In the core located outside the DNAPL source zone, DNAPL was not observed at or near the mudstone surface.

Trichloroethene concentrations in the mudstone within the vicinity of the DNAPL source zone, exceeded the DNAPL threshold concentration (410 mg/kg), indicating that DNAPL had penetrated the mudstone. This observation was confirmed by positive Sudan IV test results (Figure 3). The high DNAPL entry pressures associated

with typical clay pore throat sizes precludes DNAPL invasion into the matrix and instead suggests density-driven downward transport through fractures. The presence of DNAPL at the time of coring indicates that either DNAPL migration was an active process, or that DNAPL present within the fractures was residual, but slow to dissolve due to high concentrations in the matrix caused by previous, successive fracture replenishments (Parker et al., 1997).

DNAPL was frequently observed within the upper 0.5 m of the mudstone within SN104, SN116, SN117 and SN118. At one location (SN118), DNAPL was observed almost continuously from the interface to 0.65 m into the mudstone, with an average concentration of 5160 mg/kg. Such a continuous DNAPL trail suggests that sampling occurred along a vertical DNAPL-filled fracture. The location of this profile corresponds to a topographic low in the mudstone surface, where there is greater potential for pooled DNAPL that would aid penetration. Quantification of DNAPL mass as a percentage of pore-space (2.9 and 4.7%) in the river terrace gravels above the topographic low, determined that residual, rather than pooled mass was present (Cohen et al., 1993; Pankow and Cherry, 1996). It is therefore suggested that if pooled DNAPL was present within the topographic low, then subsequent downward flow and in-situ dissolution resulted in depletion, leaving only DNAPL residual mass. At three locations (SN104, SN116 and SN117), positive DNAPL results were observed in discrete ‘spikes’ within 0.8 m of the interface. Associated residual saturation values ranged from 3% (SN104) to 9.4% (SN116) suggesting significant quantities of DNAPL within the mudstone. These observations are ascribed to the presence of DNAPL within fractures or within lateral skerry bands, the latter of which were observed coincidently with DNAPL spikes in SN104 and SN117. A further high

concentration, aqueous phase TCE spike coincident in depth with a skerry band was observed in SN118 at ~2 m below the mudstone interface. This observation suggests that skerry bands have either contained DNAPL or have been a conduit for the transport of dissolved-phase TCE. A further skerry band was observed in all cores at between 3-4 m below the mudstone surface. Whilst this 10-30 cm thick band was not coincident with high TCE concentrations, it appeared to be laterally continuous and could act as a lateral flow conduit.

Below the maximum DNAPL penetration depth in the four cores taken from the source zone, the TCE distribution was characterized by declining concentrations with depth. For purposes of comparison with a diffusion-transport model, the TCE soil core results were expressed as pore water concentrations (Figure 5). The declining concentrations generally fall within an envelope that can be explained by diffusive transport using a range of effective diffusion coefficients between $8x10^{-6}$ and $8x10^{-5}$ m^2/d. These values are typical for TCE diffusion in clays (Johnson et al., 1989; Parker et al., 2004). These diffusive trends, which appear to begin at the lower vertical extent of DNAPL penetration, suggest that either depletion of DNAPL or increased capillary resistance as a result of reduced fracture aperture, restricted further downward flow and that subsequent dissolution of the remaining residual mass diffused into the matrix producing the observed decreasing concentrations with depth. At one location (SN118) the diffusion profile was punctuated by discrete high concentration, aqueous phase spikes at 28.45 m and 30.85 m OD (Ordnance Datum), that could not be described by diffusion. It is suggested that these spikes are indicative of samples taken near to or within cross-cutting fractures that contained DNAPL or high concentration aqueous phase TCE.

In SN120, the core that was located outside the DNAPL source zone (Figure 3), the concentration profile through the mudstone was characterized not by diffusion, but by continuously high aqueous phase concentrations to ~30.5 m OD (average 220 mg/kg or 553 mg/l). One sample at 31.88 m had a concentration of 730 mg/kg, suggesting that DNAPL was present, however the equivalent Sudan IV test was negative[1]. Two possible transport phenomena are suggested; i) that the core had been subject to matrix diffusion from an adjacent DNAPL-filled fracture or ii) that the core had been subject to matrix diffusion from a fracture containing aqueous phase TCE. Interestingly, the concentration declined rapidly after 30.5 m OD; a depth that was coincident with the laterally continuous skerry band. This evidence suggests there may be significant flow through the band, although this has not been measured; it is possible that declining concentrations were a result of flow through that conduit. A summary of TCE mass in the cores is presented in Table 2.

The degradation products of TCE including both cDCE and VC were observed within the mudstone. Samples of the mudstone were analysed for DNA to determine whether these daughter products could be present as a result of in-situ degradation. Extremely low concentrations (max. of 100 copies/g) of vinyl chloride reductase genes were determined in 17% of samples (n =18), suggesting that the bacterial population was limited. It is unknown whether this DNA resided within the fractures, skerries or the matrix, however the latter is unlikely given the typical pore throat sizes. It is uncertain

[1] Sudan IV was generally a good indicator of DNAPL presence, however inconsistencies were apparent between the Sudan IV results and the calculated DNAPL threshold levels within the mudstone of SN104, SN117 and, as discussed above, SN120. It is possible that the discrepancies are a result of either misidentification of the dissolution of red Sudan IV dye within the red mudstone matrix, the uncertainty in the parameters used in the partitioning calculation, or the presence of a mixed NAPL, characterised by a lower effective solubility, than assumed herein.

whether the presence of daughter products was a result of degradation within fractures or as a result of inward diffusion from the overlying terrace gravels.

4.2 Secondary source zone formation

Prior to remediation, TCE concentrations in three cores drilled within the source area through the river terrace gravel and first metre of the mudstone (positions shown by black dots in Figure 3) showed that concentrations in the gravels were similar to those in the mudstone (Figure 6a). Subsequently, enhanced in situ bioremediation of the gravels was performed over a two-year period removing around half of the TCE mass in the overlying aquifer (data not shown). Following this period, the source zone was re-cored (positions shown by white-filled dots in Figure 3) and total TCE soil concentrations were re-analysed. The total TCE soil concentrations within the shallow aquifer were ~45 times lower (median value) than those in the mudstone (Figure 6b). Assuming that aqueous concentrations can be inferred from the TCE soil concentrations, an upward concentration gradient is present across the mudstone interface, thereby suggesting that the mudstone will act as a secondary source that will recontaminate the overlying aquifer via diffusion.

4.3 Recontamination potential

The frequency or aperture of vertical fractures intersecting the interface cannot be known with any certainty. Therefore we use numerical modelling and sensitivity analysis of fracture properties, to understand the temporal behaviour of TCE transport out of the mudstone matrix, the mass discharge back into the overlying sediments, and the magnitude of impact that may occur in the overlying aquifer. The data collected from the analog site serve to provide a basis for fracture spacing and aperture ranges in the mudstone.

To demonstrate the importance of fracture spacing and aperture on exiting mass flux, two concentration profiles were imposed on three scenarios comprising synthetic networks of fully-penetrating vertical fractures and one scenario comprising no fractures (Cases 1 to 4 in Table 4). The two TCE profile types observed in the upper 4 m of mudstone include: log-linear decay from the mudstone interface and depth-uniform penetration suggestive of proximal contaminant 'charged' vertical fractures. The combinations of these fracture and concentration profiles are justified in Table 3. The simulations assume that dissolution of DNAPL within the mudstone is complete prior to the reversal of concentration gradients. Fracture aperture values between 50 and 100 μm and spacing values between 0.1 and 0.5 m were chosen to determine the relative effect on flux. Other model parameters are given in Table 1.

Both cumulative and instantaneous mass flux was significantly greater for the constant concentration initial profile (Figure 7a, b, c, d) compared to the diffusion-profile (Figure 7e, f, g, h), due to greater total mass in the former (13.86 mass units) compared to the latter (1.731 mass units) concentration profile. During early time periods, maximum outward flux occurred under conditions of steepest concentration gradient between the mudstone and river terrace gravels. For the non-fractured mudstone scenarios, steep concentration gradients are restricted to the upper mudstone surface only and therefore early-time fluxes are lower than in fractured scenarios where greater surface area is provided by fracture walls (Figure 7a and b). This additional surface area results in amplified initial fluxes as a larger proportion of the matrix is influenced by steep concentration gradients (Figure 7b and c). Scenarios with closer and larger aperture fractures have more exposed surface area and

increased flow, which results in lower concentrations in the fractures and steeper concentration gradients, hence greater flux (Table 4 and Figure 7d).

The rate at which instantaneous flux declines depends on the path length of diffusion. Where fractures occur at high density, matrix blocks – and therefore diffusion lengths – are small, the result is more rapid mass depletion, and therefore initially higher but earlier decrease in instantaneous flux (Figure 7d). In contrast, where fracture density is low (or fractures are absent), longer diffusion distances result in increasingly shallower concentration gradients. Therefore, mass depletion flux is slow and the decrease in instantaneous flux is attenuated (Figure 7a). It therefore follows that contaminant mass diffusion from highly fractured mudstone will shorten the secondary source lifetime to possibly single digit years. Conversely, diffusion from unfractured mudstone may represent a source of contamination for decades or centuries.

These synthetic fracture properties therefore indicate that mass removal timescales vary by one order of magnitude for the diffusion case and over three orders of magnitude for the constant concentration scenario. Given that fracture distributions and properties are rarely characterized at sites, this timescale range has significant consequences for remediation planning in the short- and long-term. To understand whether this variation is indicative of real sites, fracture properties at the analog site were studied.

4.4 Field-scale heterogeneity in fracture properties

A bimodal fracture population was observed in the man-made drainage ditch wall distinguished on the basis of aperture, spacing and infilling material. The first is a minor fracture set typified by close spacings, small, open apertures less than 100 μm and trace lengths that were generally short (~cm-scale) or unknown. The minor fractures did not appear to be continuous across the width of the drainage ditch, but their high frequency hindered confirmation. The fractures were assumed to be naturally-occurring as they appeared to continue into the mudstone perpendicular to the ditch and had similar strikes to the major fractures. They were not observed on the mudstone surface, but this is likely due to smearing of the clay during the removal of sand and gravel. The other dominant major fracture set comprised large apertures that could be traced to the base of the 1.5 m deep ditch (Figure 8a and b). These major fractures were visible over the ~12 m^2 area that was cleared of overlying sands and gravels to the west of the ditch. In plan view, the major fractures were sediment-filled and were unevenly sinuous along their horizontal length (Figure 8c and Figure 9c). Apertures ranged from 1 to 70 mm and fracture spacing ranged from 0.42 to 3.64 m (Figure 9a-b). The vertical variability of aperture and the terminal fracture depth of the major fractures was unknown. Within the north-western part of the mapped area, major fractures appeared to be absent. A summary of fracture properties is provided in Table 4.

The major fractures may have been formed as a result of the rehydration of anhydrite to gypsum. At a distance of 5 km from the industrial site, Jones (1974) observed similar-sized fractures in unsaturated mudstone to depths of >2 m below the mudstone

surface, however instead of being open, the vertical veins were filled with authigenic gypsum. The depth and connectivity of this type of fracture is critical. For fractures to be hydraulically open however, we suggest they need not penetrate the entire Mercia Mudstone Formation if instead they cross-cut 'skerry bands' that provide a hydraulic connection. Multiple horizontal skerry bands were observed within 4 m depth of the mudstone interface at the industrial site; whilst evidence for lateral flow within these was lacking, the fact that they were coincident with abrupt changes in TCE concentration suggests that they represent horizontal flow conduits. The observations by Jones (1974) of gypsum-derived minerals and solutes in the superficial deposits provides evidence for such upward flow through fractures. In addition, Firman and Dickson (1968) discuss the importance of upward flowing water for the dissolution of gypsum in low permeability deposits.

Whilst the range of fracture properties observed herein may appear atypical, fractures formed as a result of the same process occur more widely in Britain (Philipp, 2008; West, 1979), but can also be found in the Amadeus Basin, Australia (Gustavson et al., 1994), and the Newark Rift (Tabakh et al., 1998), Appalachian and the Palo Duro (Gustavson et al., 1994) Basins in the USA, although fracture apertures have not been quantified.

The presence of fractures in the weathered surface of the mudstone at the analog site, to over 1.5 m depth, supports the evidence from the industrial site that mudstone has significant potential to form a secondary source zone. If DNAPL penetration into such fractures occurred, a highly heterogeneous DNAPL distribution would be expected based on the range of fracture types and spacings observed. Similarly, following

dissolution of DNAPL and reversal of concentration gradients, spatially heterogeneous outward mass flux would also be anticipated.

4.5 Effects of field-scale heterogeneity on outward mass transport

The outward flux scenarios discussed to this point could be said to represent low permeability media with a unimodal fracture network with spacings and apertures. To evaluate the heterogeneity in recontamination potential associated with fractures measured at the analog site, those fracture properties were incorporated into the model. The duration and magnitude of mass discharge to the overlying river terrace gravel aquifer was simulated for four scenarios: A – no fractures, B - average aperture and spacing of both major and minor fracture sets observed at the quarry site, C – 10^{th} percentile (P_{10}) spacing and 90^{th} percentile (P_{90}) aperture for both fracture sets, and D – P_{90} spacing and P_{10} aperture for both fracture sets. Since the major fractures were predominantly sediment-filled, they were modelled as vertical permeable zones with a hydraulic conductivity (K) of 8.6 m/d rather than open fractures. The assigned hydraulic permeability is consistent with the overlying river terrace gravels, which are presumed to be the source of the sediment-fill. Minor fractures were defined as open and modelled using the cubic law. Other model parameters remained unchanged.

Initial TCE concentration distributions in the mudstone were defined as having either constant concentration with depth or an exponential decay with depth consistent with 1-D diffusion. All model mass flux outputs were expressed in absolute units ($g/m^2/d$) using a maximum starting TCE porewater concentration equal to solubility.

It is not surprising to find, regardless of initial TCE distribution, that the highest initial instantaneous flux occurred where unimodal large aperture fractures are closely

spaced (scenario C). Where initial TCE distributions in the mudstone were constant with depth, the initial instantaneous flux of 35 g/m^2/d (Figure 10a), decreased sharply by 3 orders of magnitude in the first year (after aquifer remediation), by which time the starting mass was nearly gone (Figure 10b). Where initial TCE concentrations in the mudstone describe a diffusion profile, early time instantaneous flux was considerably lower - 4.0 g/m^2/d (Figure 10c) - but also dropped ~3 orders of magnitude within a year, nearly exhausting the initial mass (Figure 10d). This recontamination timeframe would most likely represent a minor appendum to typical remediation timescales and as such would not pose a significant long-term problem. In contrast, where fractures are absent (scenario A), moderately spaced and of average aperture (scenario B) or widely spaced and of small aperture (scenario D), initial mass flux is low (0.3, 0.57 and 1.9 g/m^2/d, respectively, for initially constant concentration with depth and 0.13, 0.19 and 0.32 g/m^2/d, respectively, for initial diffusion profile) and may persist for 100's of years (Figure 10a and 10c). An examination of cumulative flux shows that, where initial concentrations are constant with depth (Figure 10b), it would take nearly 1000 years for just half of the initial mass to exit the mudstone if no fractures were present (scenario A). The 50% mass depletion times for unimodal moderate fracture aperture/spacing (scenario B) or narrow, widely spaced fractures (scenario D) lie between 50-100 years – considerably more than typical remediation timeframes. The 50% mass depletion times for fracture scenarios A, B and D were considerably quicker (8 - 60 years) when initial concentrations described a diffusion profile. This was a reflection of the lower total starting mass compared to the constant concentration/depth case, and that most of the mass was distributed close to the mudstone interface.

It is of course unlikely that friable low permeable media would host only closely spaced, large aperture (i.e. scenario C) fractures. Rather, it could be expected that such media would exhibit a range of fracture spacing and apertures. Simulation of mass flux from a constant concentration starting profile of contamination with a mixture of fracture types (0, 10, 20 and 50% scenario C fractures and equal proportions of scenario A, B and D fractures) shows the relative contributions of each fracture type through time (Figure 11a). Initial instantaneous fluxes were high within the first year (8 to 32 $g/m^2/d$), as mass migrated out of the closely spaced, large-aperture fractures. Thereafter instantaneous flux converged to a narrow range (for example, between 0.04-0.08 $g/m^2/d$ after 20 years) and decreased in a log linear fashion for ~1000 years. Temporal flux variation during that period was subtle, influenced by heterogeneous distribution of diffusion path lengths (due to variable fracture spacing). A similar long-term outward flux pattern resulted when similar combinations of smaller aperture fractures are used (as per the synthetic fracture modelling scenarios described above and in Table 4, cases 1 to 4), particularly after the first year (Figure 11b). Given that all the various fracture aperture/spacing combinations (both synthetic and measured) resulted in a narrow band of simulated mass flux after one year, one potential conclusion is that mass flux from a low permeability unit could be estimated without having to measure fracture properties. The simulation results presented in Figure 11 suggest that, when considering potential recontamination in a bounding aquifer, an important factor is the time elapsed since that aquifer was remediated. Also, it is clear from Figure 10 that the nature of initial concentrations in the low permeability unit influences the magnitude of outward mass flux. As such, site characterisation should seek to establish the dominant distribution type. Of course, a continuum of initial distributions may exist, particularly where

DNAPL is present. However, the simulations presented herein suggest that after a relatively short time when mass flux may vary widely across a site, flux will eventually converge to a narrow, predictable range. In the context of assessing potential re-contamination, this perhaps reduces the burden of characterisation to determining the surface area contributing contaminant mass to an aquifer (including both source and plume zone areas), the contaminant depth profile types, and the hydraulic properties of the receiving aquifer.

It is not obvious from the mass flux and discharge data shown in Figures 10 and 11 what the impact to a bounding aquifer would be in concentration terms (a more common regulatory metric). During the SABRE experiment, groundwater flowed into the three-sided cell at the up-gradient open end and was controlled by pumping from two fully screened wells at the down-gradient end at a total flow rate of 2 l/min. To estimate the magnitude of recontamination, the average concentrations that would be observed in the abstraction wells of the SABRE cell after 1 year and between 9-10, 10-20, 20-30 and 30-50 years were calculated assuming: complete mixing in the shallow aquifer; a saturated cell volume of 600 m^3, and a river terrace gravel porosity of 0.3. The DNAPL source zone occupied approximately 62% of the SABRE cell and hence for this calculation, contamination in the mudstone was assumed over this area (74 m^2). The results shown in Table 6 suggest that recontamination from the measured fracture sets at the analog site will most often start in the 5-30 mg/L range and tail down to <2 mg/L over the next 50 years, except where larger aperture, closely-spaced fractures are present. This pattern is consistent with the modelled mass flux histories, and suggests the potential for re-contamination from low permeability media could exceed regulated limits for many years. Now assume that the fractures are

heterogeneously distributed and consider the cases where 0, 10, 20 and 50% of the fractures have large aperture and close spacing (scenario C) and the remaining fractures are from the other scenarios. After the first year, the concentrations in the abstraction wells are very similar in the four heterogeneously fractured scenarios. Concentrations in the abstraction wells as a result of outward mass flux from distributions of the synthetic fractures showed similar results. This comparison suggests that if a given low permeability unit hosts a wide distribution of fracture apertures and spacing, then the outward mass flux and resulting aquifer concentration should be predictable after the first year. Such predictability should make it straightforward to manage post-remediation re-contamination. Whilst significant in terms of concentration, re-contamination of a bounding aquifer is likely to be confined within 20-30 cm of the interface (Mackay et al., 2000). As such, depending on the thickness of, and volumetric flux through, the receiving aquifer, this recontamination may not be severe enough to warrant action.

5 Conclusions

Fractured mudstones invaded by DNAPL have the potential to become significant reservoirs for VOCs that may result in recontamination of adjacent aquifers. To predict the potential magnitude and duration of recontamination, we hypothesised that it is necessary to characterise fracture aperture and spacing within secondary source zones. However, our results show that if a heterogeneous fracture distribution is assumed, outward mass flux can be predicted after the first year of recontamination. Outward flux in that first year is governed by diffusion over steep concentration gradients and short path-lengths and hence the magnitude of flux is dependent on the frequency of closely spaced fractures. After the first year, given a heterogeneous

distribution of diffusion pathlengths, outward flux is predictable within a narrow envelope of values. Potential conclusions are that mass flux could be estimated without having to measure fracture properties and that the elapsed time since the adjacent aquifer was remediated is perhaps the best indicator of outward mass flux. Our results suggest that establishing the concentration distribution in the low permeability unit is key to estimating initial flux magnitude and flux longevity, however in terms of flux, after the first year, values converge to a narrow range despite initial concentration distributions. To estimate mass flux from low permeability deposits we suggest that characterisation should focus on determining the surface area contributing contaminant mass to an aquifer, the contaminant depth profile types, and the hydraulic properties of the low permeability and receiving aquifer.

Acknowledgements

This paper is published with the permission of the Executive Director of the British Geological Survey (NERC). Work on the SABRE Project at the British Geological Survey was supported by NERC (Grant No. NE/C513193/1).

The SABRE project team comprises (in no particular order): DuPont; Honeywell; Shell Global Solutions; ESI; Terra Systems; GeoSyntec Consultants; British Geological Survey; Acetate Products; Golder Associates; Scientifics; University of Sheffield; Akzo Nobel; University of Edinburgh; General Electric and CL:AIRE.

The SABRE project team would like to acknowledge the in-kind and direct financial contributions made by each participating organisation. SABRE is funded through the DTI Bioremediation LINK programme (http://www.clarrc.ed.ac.uk/link/) with specific financial contributions from BBSRC, DTI, the Environment Agency, EPSRC and NERC, which are gratefully acknowledged.

Figure 1 Conceptual diagram showing a) inward DNAPL transport and subsequent dissolution, followed by matrix diffusion in the aqueous phase from the adjacent aquifer into the low permeability deposit and b) outward aqueous phase transport from the low permeability deposit back into the adjacent aquifer

Figure 2 Location of the industrial site and analog site within a shallow river valley system

Figure 3 Core location map. Named boreholes represent positions of TCE profiles within lower river terrace gravel shallow aquifer and mudstone. Black-filled and white-filled points within SABRE test cell represent cores taken through river terrace gravels and upper mudstone pre- and post-remediation respectively. Black cross represents location of multilevel sampler where DNAPL was pumped from base of river terrace gravels. Graphs show TCE profiles within lower river terrace gravels and mudstone. Black-filled points denote negative Sudan IV test results, white-filled points denote positive Sudan IV test results.

Figure 4 Schematic of mudstone model domain showing flow boundaries, example fracture distribution and initial concentration profiles

Figure 5 Profiles of calculated TCE pore water concentrations compared to synthetic 1-D diffusion fronts calculated with effective diffusion coefficients of 1e-10 , 5e-10 and 1e-9 m^2/d

Figure 6 TCE profiles obtained from solid core analysis above and below the mudstone interface pre- and post-enhanced bioremediation targeted at the river terrace gravel aquifer. Individual symbols represent single cores.

Figure 7 Plots of instantaneous and cumulative flux calculated at boundary of mudstone and river terrace gravels. Plots a and e represent simulations without fractures. All other plots represent simulations with unimodal fracture distributions with characteristics including; 0.5 m spaced, 50 µm aperture (b, f); 0.1 m spaced, 50 µm 2b (c,g) and 0.1 m spaced, 100 µm 2b (d,h). Column 1 shows results where initial concentration profile was constant concentration with depth, column 2 shows results where initial concentration profile was a diffusion profile

Figure 8 Fractures observed at Site B including a) major fractures observed in the drainage ditch wall, b) fractures extending to >1.5 m depth and c) sediment-filled fractures in plan view adjacent to drainage ditch

Figure 9 a) Fracture spacings and b) fracture apertures measured at the analog field site (box plot represents 10^{th}, 25^{th}, 75^{th} and 90^{th} percentiles, median (solid line) and the mean (dashed line); c) plan view of major fractures mapped on the mudstone surface and within the drainage ditch, with perpendicular bars showing variation in aperture

Figure 10 Simulation results with different initial concentration distributions, including; a) instantaneous flux from a constant concentration profile; b) cumulative discharge from a constant concentration profile; c) instantaneous flux from a diffusion profile, and d) cumulative discharge from a diffusion profile. Scenario A) diffusion only (no fractures), Scenario B) Set 1; 2b 17 mm, Sp 2.08 m, et 2; 2b 0.035 mm, Sp 0.63 m); scenario C) Set 1; 2b 49 mm, Sp 0.567 m, Set 2; 2b 0.1 mm, Sp 0.047 m), and scenario D) Set 1; 2b 5 mm, Sp 3.37 m, Set 2; 2b 0.01 mm, Sp 1.726 m)

Figure 11 Instantaneous flux from mudstone fractured with differing proportions of fractures, namely: a) 0%, 10%, 20% and 50% of scenario C fractures and equal proportions of scenario A, B and D fractures and b) 0%, 10%, 20% and 50% of 0.1 mm. 0.1 m spaced fractures and equal proportions of 0.050 mm/0.1 m, 0.050 mm/0.5 m, no fractures. Initial contaminant profile: constant concentration with depth

Table 1 Model input parameters used in Fractran simulations

Table 2 Summary of average TCE mass, TCE DNAPL volume and depth of DNAPL penetration in the five cores collected from the mudstone.

Table 3 Justifications for contaminant distributions within fractured/non-fractured model domain

Table 4 Summary of model domain hydraulic properties for each of the 8 fractured/non-fractured mudstone scenarios. P_{10}: 10^{th} percentile, P_{90}: 90^{th} percentile

Table 5 Summary of bi-modal fracture network at the analog site

Table 6 Average concentration (mg/l) in the abstraction well of the SABRE cell over time periods of up to 1 year and between 1 and 10, 10 and 20, 20 and 30, and 30 and 50 years for cases where the initial concentration profile is constant with depth or a diffusion profile and where fractures present are case A, B, C and D or distributions of these fractures containing 0, 10, 20 or 50% of scenario C fractures and equal proportions of the other scenarios. Where values are not present, concentrations are <0.3 mg/l.

Aljubouri, Z., 1971. Sedimentary Structures preserved in fibrous gypsum veins near Gunthorpe Weir, Nottinghamshire. Mercian Geologist, 4(1): 9-11.

Allen-King, R., McKay, L. and Trudell, M., 1997. Organic carbon dominated trichloroethene sorption in a clay-rich glacial deposit. Ground Water, 35(1): 124-130.

Allen, D. et al., 1997. The physical properties of major aquifers in England and Wales, British Geological Survey

Buss, S. et al., 2010. Project Sabre (Source Area BioRemediation) - an Overview, Contaminated Land: Applications in Real Environments.

Chambon, J., 2010. Modeling multi-component transport and enhanced anaerobic dechlorination processes in a single fracture-clay matrix system. Journal of Contaminant Hydrology, 112: 77-90.

Chapman, S.W. and Parker, B.L., 2005. Plume persistence due to aquitard back diffusion following dense nonaqueous phase liquid source removal or isolation. Water Resources Research, 41(12).

Christiansen, C. et al., 2008. Characterization and quantification of pneumatic fracturing effects at a clay till site. Environmental Science and Technology, 42: 570-576.

Cohen, R., Mercer, J. and Matthews, J., 1993. DNAPL site evaluation. CRC Press, Boca Raton, Florida.

Doherty, R., 2000. A history of the production and use of carbon tetrachloride, tetrachloroethylene, trichloroethylene and 1,1,1-trichloroethane in the United States: Part 2 -Trichloroethylene and 1,1,1-trichloroethane. Environmental Forensics, 1(2): 83-93.

Espositio, S. and Thomson, N., 1999. Two-phase flow and transport in a single fracture-porous medium system. Journal of Contaminant Hydrology, 37: 319-341.

Falta, R.W., 2004. Dissolved chemical discharge from fractured clay aquitards contaminated by DNAPLs. In: B. Faybishenko, P.A. Witherspoon and J. Gale (Editors), 2nd International Symposium on Dynamics of Fluids in Fractured Rock, Berkeley, CA, pp. 165-174.

Feenstra, S., Cherry, J.A. and Parker, B.L., 1996. Conceptual models for the behavior of dense non-aqueous phase liquids (DNAPLs) in the subsurface. In: J. Pankow and J.A. Cherry (Editors), Dense Chlorinated Solvents and Other DNAPLs in Groundwater. Waterloo, Portland, Oregan, pp. 53-88.

Feenstra, S., Mackay, D. and Cherry, J., 1991. A method for assessing residual NAPL based on organic-chemical concentrations in soil samples. Ground Water Monitoring and Remediation, 11(2): 128-136.

Firman, R. and Dickson, J., 1968. The solution of gypsum and limeston by upward flowing water. Mercian Geologist, 4: 401-408.

Gerhard, J., Pang, T. and Kueper, B., 2006. Time scales of DNAPL migration in sandy aquifers examined via numerical simulation. Ground Water, 45(2): 147-157.

Gustavson, T., Hovorka, S. and Dutton, A., 1994. Origin of satin spar veins in evaporite basins. Journal of Sedimentary Research, A64(1): 88-94.

Hobbs, P. et al., 2002. Engineering geology of British Rocks and Soils - Mudstones of the Mercia Mudstone Group. RR/01/02, British Geological Survey, Keyworth.

Hønning, J., Broholm, M. and Bjerg, P., 2007. Role of diffusion in chemical oxidation of PCE in a dual permeability system. Environmental Science and Technology, 41: 8426-8432.

Johnson, R., Cherry, J. and Pankow, J., 1989. Diffusive contaminant transport in natural clay: A field example and implications for clay-lined waste disposal sites. Environmental Science and Technology, 23(3): 340-349.

Jones, H. et al., 2000. The physical properties of minor aquifers in England and Wales, Environment Agency R&D Publication 68.

Jones, P., 1974. An occurrence of authigenic gypsum in Pleistocene till at Boulton Moor near Derby. The Mercian Geologist, 5(2): 163-174.

Kimblin, R.T., 1995. The chemistry and origin of groundwater in Triassic Sandstone and Quaternary deposits, Northwest England and some UK comparisons Journal of Hydrology, 172(1-4): 293-311.

Kueper, B. and McWhorter, D.B., 1991. The behaviour of dense, nonaqueous phase liquids in fractured clay and rock. Ground Water, 29(5): 716-728.

Liu, C. and Ball, W., 2002. Back diffusion of chlorinated solvent contaminants from a natural aquitard to a remediated aquifer under well-controlled field conditions: Predictions and measurements Ground Water, 40(2): 175-184.

Mackay, D. and Cherry, J.A., 1989. Groundwater contamination- pump-and-treat remediation 2. Environmental Science and Technology, 23(6): 630-636.

Mackay, D. et al., 2000. A controlled field evaluation of continuous vs. pulsed pump-and-treat remediation of a VOC-contaminated aquifer: site characterization, experimental setup and overview of results. Journal of Contaminant Hydrology, 41(1-2): 81-131.

Maymo-Gatell, X., Chien, Y., Gossett, J. and Zinder, S., 1997. Isolation of a bacterium that reductively dechlorinates tetrachloroethene to ethene. Science, 276(5318): 1568-1571.

Mercer, J. and Cohen, R., 1990. A review of immiscible fluids in the subsurface: properties, models, characterization and remediation. Journal of Contaminant Hydrology, 6(2): 107-164.

Murray, R., 1964. Origin and diagenesis of gypsum and anhydrite. Journal of Sedimentary Petrology, 34: 512-523.

Mutch, R., Scott, J. and Wilson, D., 1993. Cleanup of fractured rock aquifers: Implications of matrix diffusion. Environmental Monitoring and Assessment, 24: 45-70.

Pankow, J. and Cherry, J.A., 1996. Dense chlorinated solvents and other DNAPLs in groundwater: history, behaviour, and remediation. Waterloo Press, Portland, Oregan.

Parker, B., Cherry, J., Chapman, S. and Guilbeault, M., 2003. Review and analysis of chlorinated solvent dense nonaqueous phase liquid distributions in five sandy aquifers. Vadose Zone Journal, 2: 116-137.

Parker, B.L., Chapman, S.W. and Guilbeault, M.A., 2008. Plume persistence caused by back diffusion from thin clay layers in a sand aquifer following TCE source-zone hydraulic isolation. Journal of Contaminant Hydrology, 102(1-2): 86-104.

Parker, B.L., Cherry, J.A. and Chapman, S.W., 2004. Field study of TCE diffusion profiles below DNAPL to assess aquitard integrity. Journal of Contaminant Hydrology, 74(1-4): 197-230.

Parker, B.L., Gillham, R.W. and Cherry, J.A., 1994. Diffusive disappearance of immiscible-phase organic liquids in fractured geologic media Ground Water, 32(5): 805-820.

Parker, B.L., McWhorter, D.B. and Cherry, J.A., 1997. Diffusive loss of non-aqueous phase organic solvents from idealized fracture networks in geologic media. Ground Water, 35(6): 1077-1088.

Philipp, S., 2008. Geometry and formation of gypsum veins in mudstones at Watchet, Somerset, SW England. Geological Magazine, 145(6): 831-844.

Reynolds, D. and Kueper, B., 2004. Multiphase flow and transport through fractured heterogeneous porous media Journal of Contaminant Hydrology, 71: 89-110.

Sale, T., Zimbron, J. and Dandy, D., 2008. Effects of reduced contaminant loading on downgradient water quality in an idealized two-layer granular media. Journal of Contaminant Hydrology, 102: 72-85.

Scheutz, C. et al., 2008. Concurrent ethene generation and growth of Dehalococcoides containing vinyl chloride reductive dehalogenase genes during a stimulated reductive dechlorination field demonstration. Environmental Science and Technology, 42: 9302-9309.

Seedhouse, R.L. and Sanders, R.L., 1990. Investigations for cooling-tower foundations in Mercia Mudstone at Ratcliffe-on-Soar, Nottingham In: J.C. Cripps et al. (Editors), 26th Annual Conf of the Engineering Group of the Geological Soc : Engineering Geology of Weak Rock. A a Balkema, Leeds, England, pp. 465-471.

Shearman, D., Mossop, G., Dunsmore, H. and Martin, H., 1972. Origin of Gypsum veins by hydraulic fracture. Transactions of the institute of mining and metallurgy Section B Applied Earth Sciences(81): 149-55.

Slack, W., Murdoch, L. and Meiggs, T., 2000. Hydraulic fracturing to improve in situ remediation. In: G. Wickramanayake, A. Gavaskar and A. Chen (Editors), 2nd International Conference on Remediation of Chlorinated and Recalcitrant Compounds. Battelle Press, Monterey, pp. 291-298.

Sudicky, E., 1989. The Laplace transform Galerkin technique: A time-continuous finite element theory and application to mass transport in groundwater. Water Resources Research, 25(8): 1833-1846.

Sudicky, E. and McLaren, R., 1992. The Laplace Transform Galerkin technique for large scale simulation of mass transport in discretely fractured porous formations. Water Resources Research, 28(499-514).

Tabakh, M., Schreiber, B. and Warren, J., 1998. Origin of fibrous gypsum in the Newark Rift Basin, Eastern North America. Journal of Sedimentary Research, 68(1): 88-99.

Tellam, J. and Lloyd, J., 1981. Hydrogeology of British onshore non-carbonate mudrocks. Quarterly Journal of Engineering Geology, 14: 347-355.

USEPA, 1994. Alternative methods for fluid delivery and recovery. EPA/625/R-94/003, U.S. Environmental Protection Agency, Washington DC.

USEPA, 2003. Volatile organic compounds in various sample matrices using equilibrium headspace analysis. In: M. 5021A (Editor), Test Methods for evaluating solid waste, physical/chemical methods (SW-846). USEPA.

West, I., 1979. Review of evaporite diagenesis in the Purbeck Formation of Southern England, Sedimentation Jurassique W. Europeen. ASF Publication speciale. Association des Sédimentologistes Français, pp. 407-416.

White, R., 2007. Organic contaminant transport through a thin clay aquitard influenced by palaeo-heterogeneities. PhD Thesis, University of Birmingham, Birmingham, 438 pp.

Wilson, A.A., 2003. The Mercia Mudstone Group (Triassic) of Manchester Airport, Second Runway. Proceedings of the Yorkshire Geological Society, 54: 129-145.

Table 7 Model input parameters used in Fractran simulations

Parameter	**Value**	**Source**
Hydraulic conductivity	$9x10^{-6}$ m/d	(Tellam and Lloyd, 1981)
Dispersivity	0.1m in fractures 0 in mudstone	(Jørgensen et al., 1998)
Effective diffusion coefficient (D^*) [1]	0.00003 m^2/d	Calculated
Porosity	0.29	Calculated as discussed earlier
Retardation	2.31	Calculated using field-derived f_{oc}; 0.002, K_{oc}; 113 l/kg (Fetter, 1999)
Bulk density	1.68 g/cm^3	(Hobbs et al., 2002)
Vertical hydraulic gradient	0.02	Measured
Free solution diffusion coefficient (D_d)	6.1×10^{-5} m^2/d	(Geankoplis, 1993)
Fluid density	0.999 g/cm^3	(Lide, 1994)

[1] $D^* = D_d \tau$, where apparent tortuosity (τ) is 0.48; similar τ values have been reported by, or calculated from, McKay et al. (1993), Desaulniers (1986) and Barone et al. (1989).

Table 8 Summary of average TCE mass, TCE DNAPL volume and depth of DNAPL penetration in the five cores collected from the mudstone.

Core (SN)	Did core contain DNAPL?	Profile type	TCE (kg)	Core TCE mass (kg/m^3)	% TCE as DNAPL	Volume DNAPL per core (ml)	DNAPL penetration depth (m)
104	Yes	Diffusion	0.0096	0.53	80	5.3	0.6
116	Yes	Diffusion	0.0292	1.57	96	19.2	0.45
117	Maybe	Diffusion	0.0126	0.58	83	7.2	0.65
118	Yes	Diffusion	0.0406	1.38	98	27.3	1.35
120	No	Advection	0.0082	0.30	7	0	0

Table 9 Justifications for contaminant distributions within fractured/non-fractured model domain

	Diffusion profile	Constant concentration profile
Non-fractured	Dissolved-phase transport across the concentration gradient at the interface	Possible where DNAPL penetrates dead-end fractures*
Fractured	Contaminant distribution unlikely, but included to represent a fractured scenario with minimal contamination	Possible where DNAPL or the aqueous phase penetrates fractures with subsequent matrix diffusion

*Flow velocities in dead-end fractures are low such that fracture flow does not significantly contribute to outward flux. Hence following dissolution of the DNAPL, back diffusion from the fractured matrix is similar to that where fractures are absent (White, 2007)

Table 10 Summary of model domain hydraulic properties for each of the 8 fractured/non-fractured mudstone scenarios. P_{10}: 10^{th} percentile, P_{90}: 90^{th} percentile

Case number	**Type[1]**	**Fracture spacing (m)**	**Fracture 2b (μm)**	**Fracture transmissivity (m^2/d)**	**No. of fractures per m**	**Q_{frac} (m^3/d)**	**Q_{tot} (m^3/d)**
1	S	0	0	-	0	-	$3.4x10^{-5}$
2	S	0.10	50	$8.8x10^{-3}$	10	$7.1x10^{-3}$	$7.1x10^{-3}$
3	S	0.50	50	$8.8x10^{-3}$	2	$1.4x10^{-3}$	$1.4x10^{-3}$
4	S	0.10	100	$7.1x10^{-2}$	10	$5.7x10^{-2}$	$5.7x10^{-2}$
5	F	Scenario A (no fractures)		-	0	-	$3.4x10^{-5}$
6	F	Scenario B (average properties)		4	4	$3.2x10^{-3}$	$3.2x10^{-3}$
7	F	Scenario C (P_{10} spacing, P_{90} aperture)		96	13	$2.55x10^{-2}$	$2.55x10^{-2}$
8	F	Scenario D (P_{90} spacing, P_{10} aperture)		0.1	3	$0.9x10^{-3}$	$0.9x10^{-3}$

[1]S: Synthetic fracture set, F: Fracture set derived from field measurements.

Table 11 Summary of bi-modal fracture network at the analog site

	Average	Range	P_{10} values	P_{90} values	Comments
Major fracture properties					
Aperture (mm)	17	1-70	5	49	Sand and gravel filled
Spacing (m)	2.08	0.42-3.64	0.567	3.37	
Minor fracture properties					
Aperture (mm)	~0.035	<0.1	0.01	0.1	Observed in ditch only
Spacing (m)	0.63	0.02-2.14	0.047	1.726	

Table 12 Average concentration (mg/l) in the abstraction well of the SABRE cell over time periods of up to 1 year and between 1 and 10, 10 and 20, 20 and 30, and 30 and 50 years for cases where the initial concentration profile is constant with depth or a diffusion profile and where fractures present are scenario A, B, C and D or distributions of these fractures containing 0, 10, 20 or 50% of scenario C fractures and equal proportions of the other scenarios. Where values are not present, concentrations are <0.3 mg/l.

Time (yrs)	A	B	C	D	0% C	10% C	20% C	50% C
Constant concentration with depth								
0-1	4.3	28.8	293	12.1	15.1	22.5	30.0	51.5
1-10	1.3	9.0		4.8	5.1	5.5	6.0	7.2
10-20	0.7	5.0		2.6	2.8	2.5	2.2	1.2
20-30	0.6	3.6		1.9	2.0	1.8	1.6	0.9
30-50	0.5	2.3		1.4	1.4	1.3	1.1	0.6
Diffusion profile								
0-1	3.9	9.0	60*	5.6	6.2	9.2	12.2	20.8
1-10	0.9	1.9		1.3	1.4	1.2	1.1	0.6
10-20	0.4	0.6		0.49	0.48	0.43	0.38	0.21
20-30	0.2	0.2		0.29	0.25	0.22	0.20	0.1
30-50	0.1	0.1		0.17	0.13	0.12	0.10	0.05

*Calculated average over 0.5 years

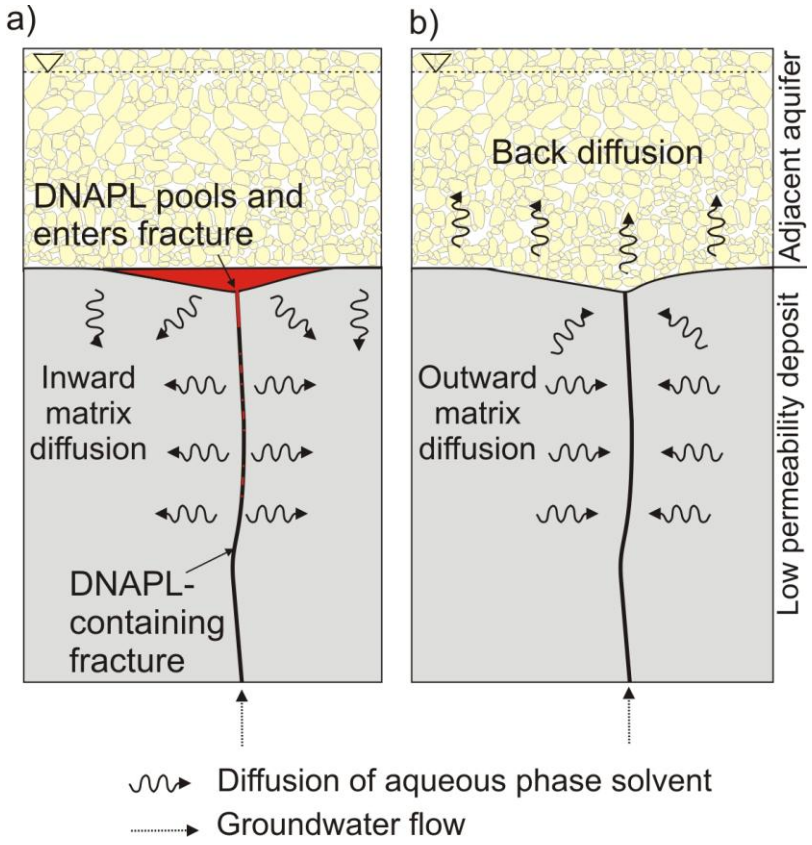

Figure 12 Conceptual diagram showing a) inward DNAPL transport and subsequent dissolution, followed by matrix diffusion in the aqueous phase from the adjacent aquifer into the low permeability deposit and b) outward aqueous phase transport from the low permeability deposit back into the adjacent aquifer

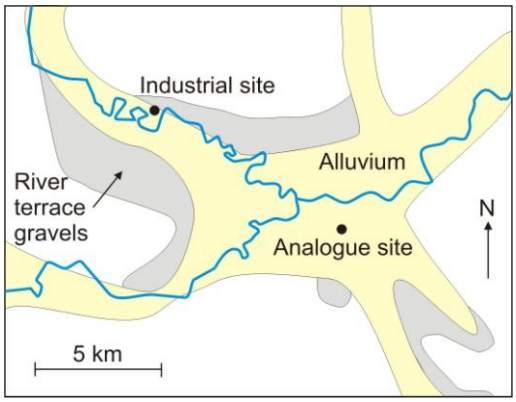

Figure 13 Location of the industrial site and analog site within a shallow river valley system

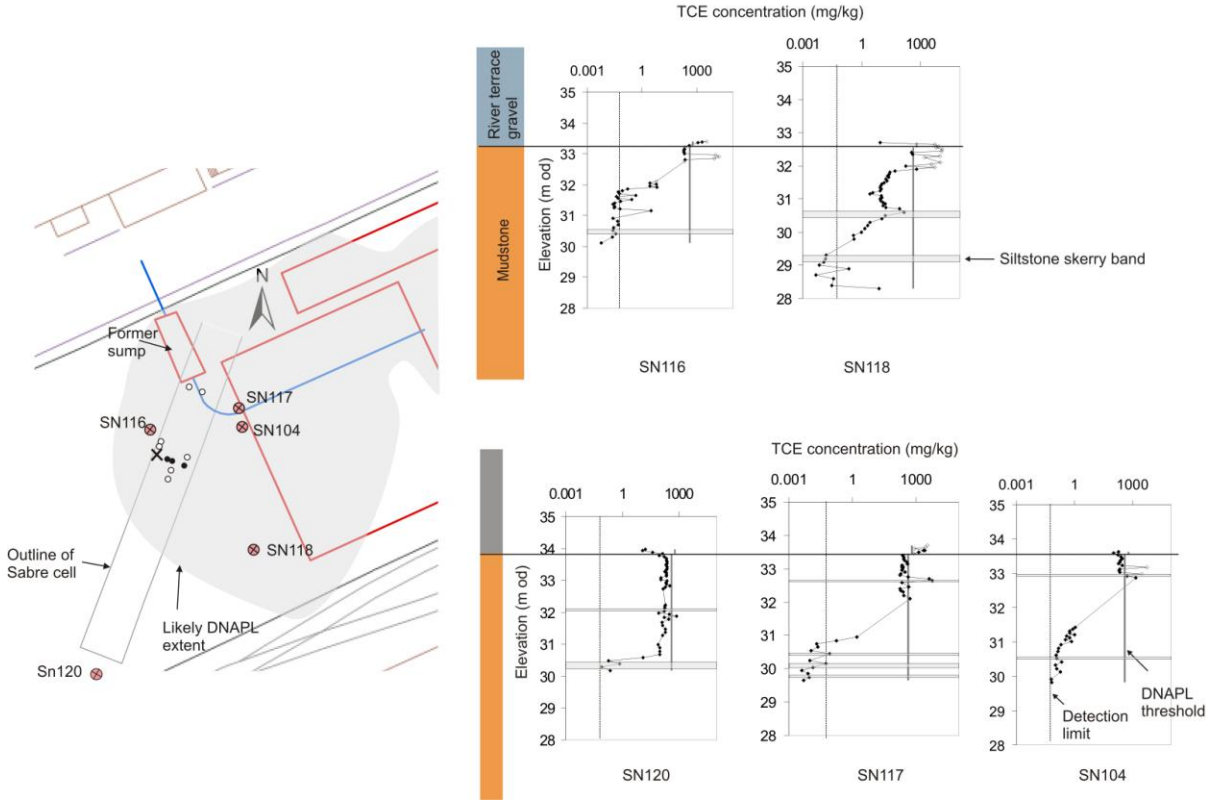

Figure 14 Core location map. Named boreholes represent positions of TCE profiles within lower river terrace gravel shallow aquifer and mudstone. Black-filled and white-filled points within SABRE test cell represent cores taken through river terrace gravels and upper mudstone pre- and post-remediation respectively. Black cross represents location of multilevel sampler where DNAPL was pumped from base of river terrace gravels. Graphs show TCE profiles within lower river terrace gravels and mudstone. Black-filled points denote negative Sudan IV test results, white-filled points denote positive Sudan IV test results.

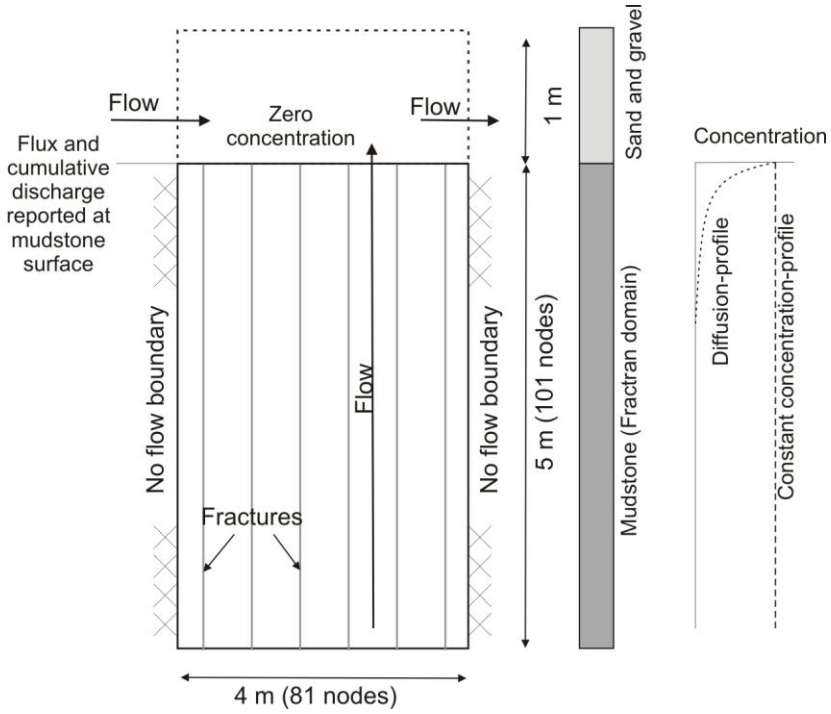

Figure 15 Schematic of mudstone model domain showing flow boundaries, example fracture distribution and initial concentration profiles

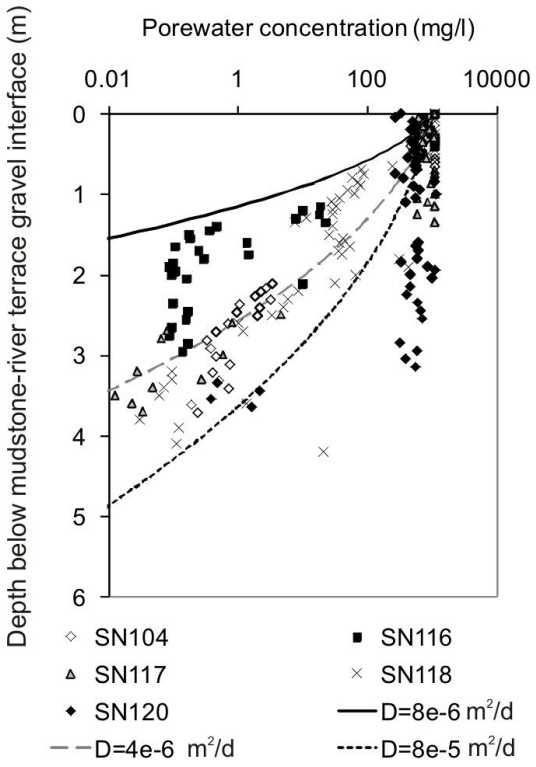

Figure 16 Profiles of calculated TCE pore water concentrations compared to synthetic 1-D diffusion fronts calculated with effective diffusion coefficients of 1e-10 , 5e-10 and 1e-9 m^2/d

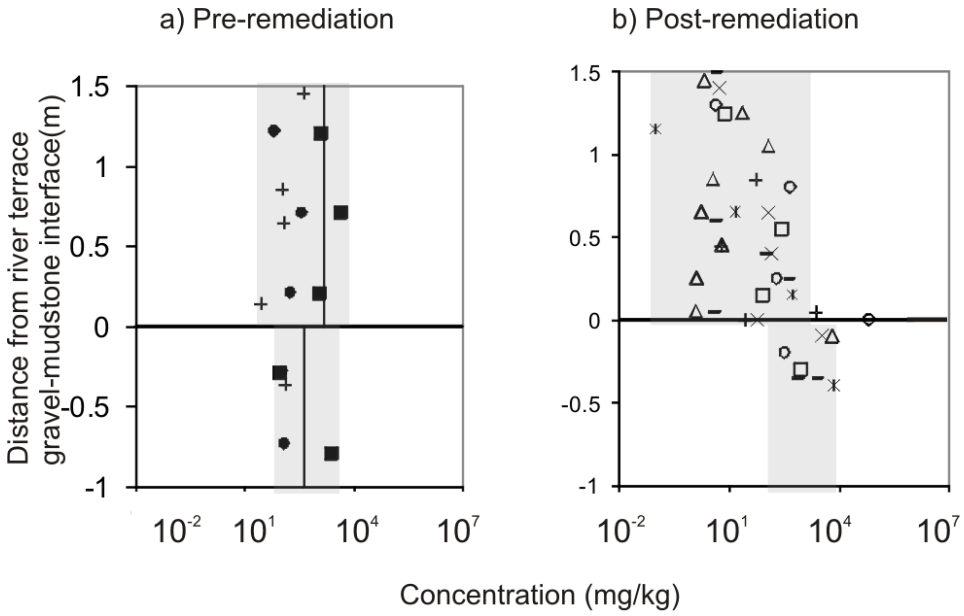

Figure 17 TCE profiles obtained from solid core analysis above and below the mudstone interface pre- and post-enhanced bioremediation targeted at the river terrace gravel aquifer. Individual symbols represent single cores.

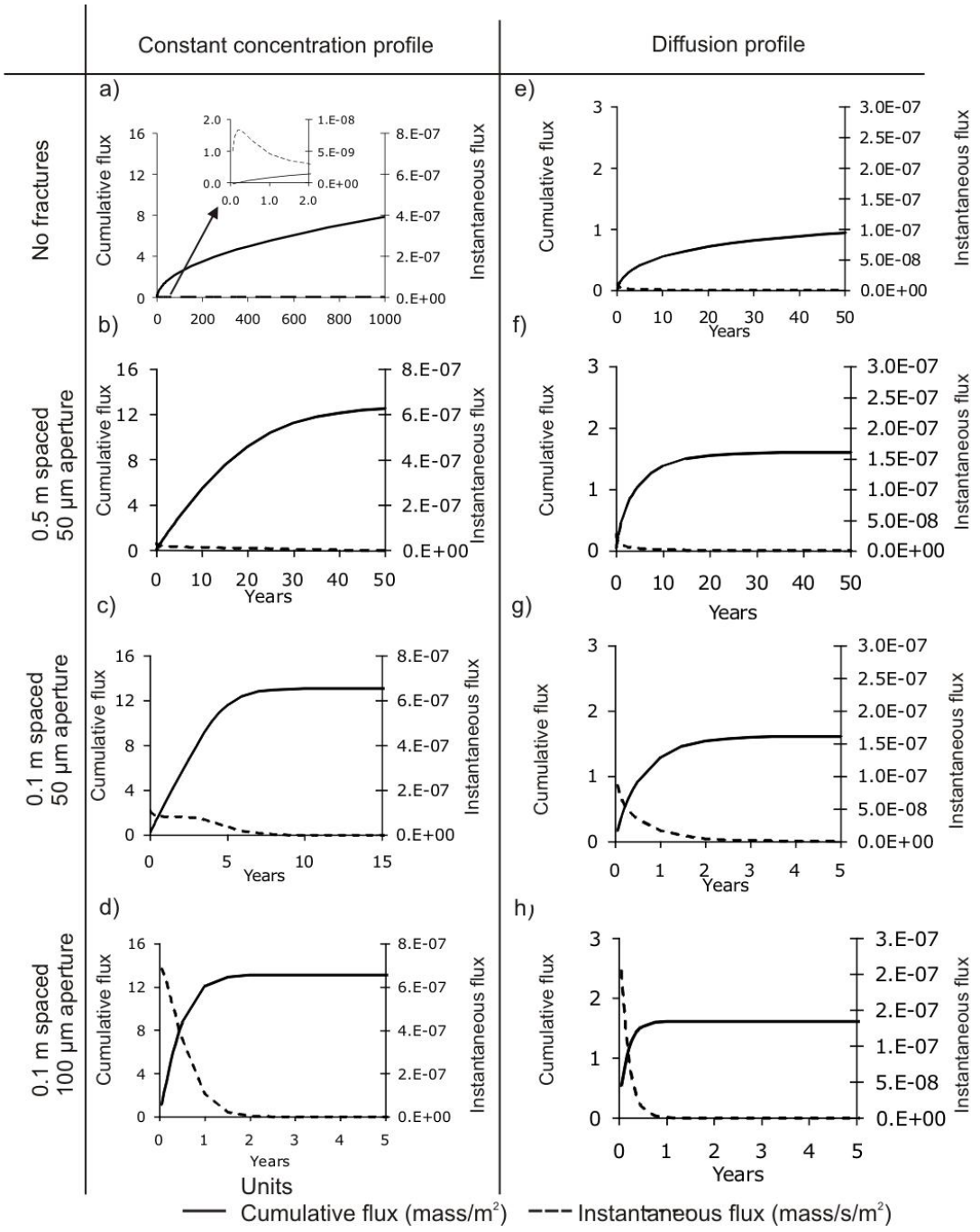

Figure 18 Plots of instantaneous and cumulative flux calculated at boundary of mudstone and river terrace gravels. Plots a and e represent simulations without fractures. All other plots represent simulations with unimodal fracture distributions with characteristics including; 0.5 m spaced, 50 µm aperture (b, f); 0.1 m spaced, 50 µm 2b (c,g) and 0.1 m spaced, 100 µm 2b (d,h). Column 1 shows results where initial concentration profile was constant concentration with depth, column 2 shows results where initial concentration profile was a diffusion profile

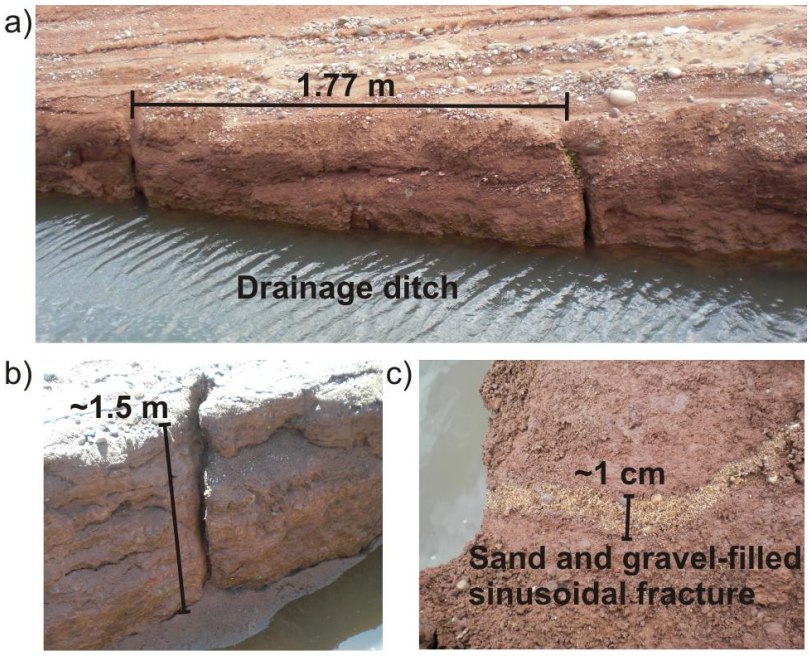

Figure 19 Fractures observed at Site B including a) major fractures observed in the drainage ditch wall, b) fractures extending to >1.5 m depth and c) sediment-filled fractures in plan view adjacent to drainage ditch

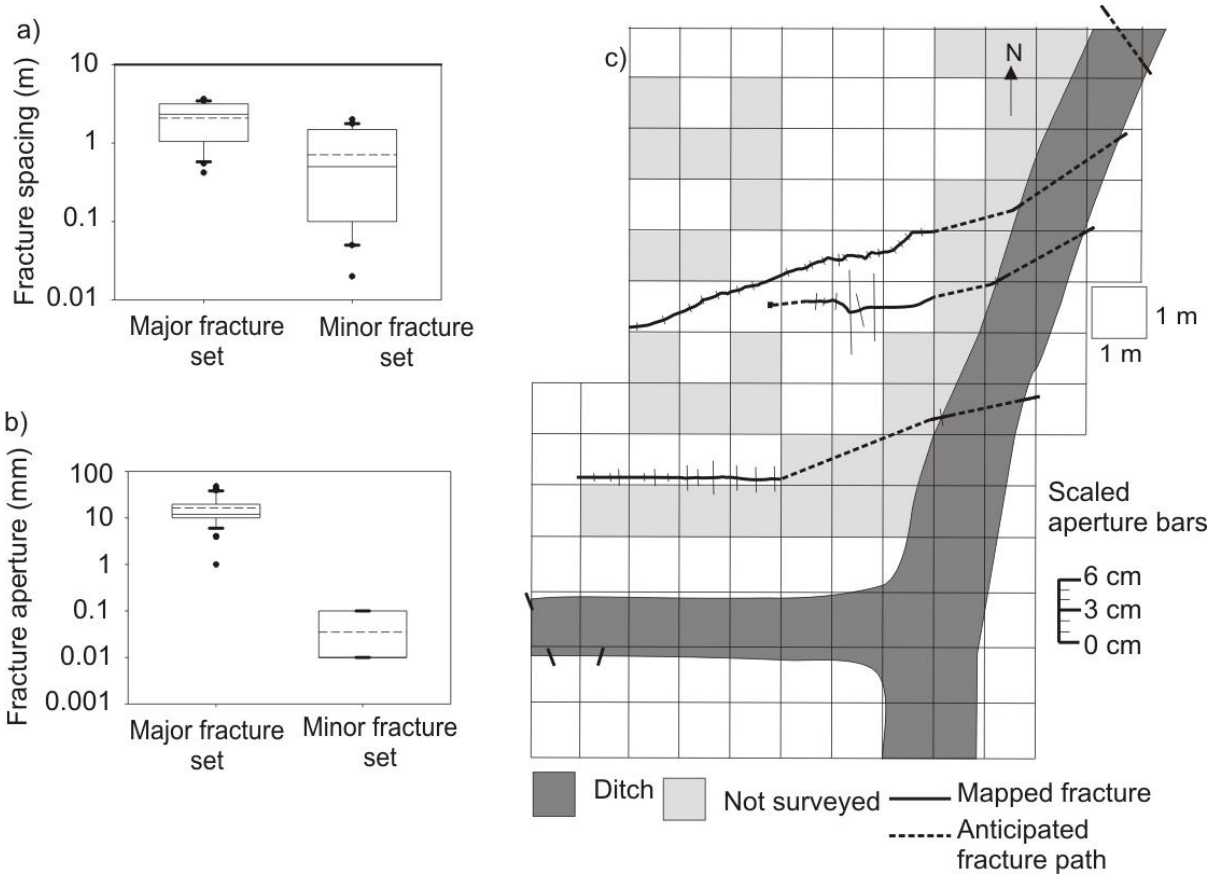

Figure 20 a) Fracture spacings and b) fracture apertures measured at the analog field site (box plot represents 10th, 25th, 75th and 90th percentiles, median (solid line) and the mean (dashed line); c) plan view of major fractures mapped on the mudstone surface and within the drainage ditch, with perpendicular bars showing variation in aperture

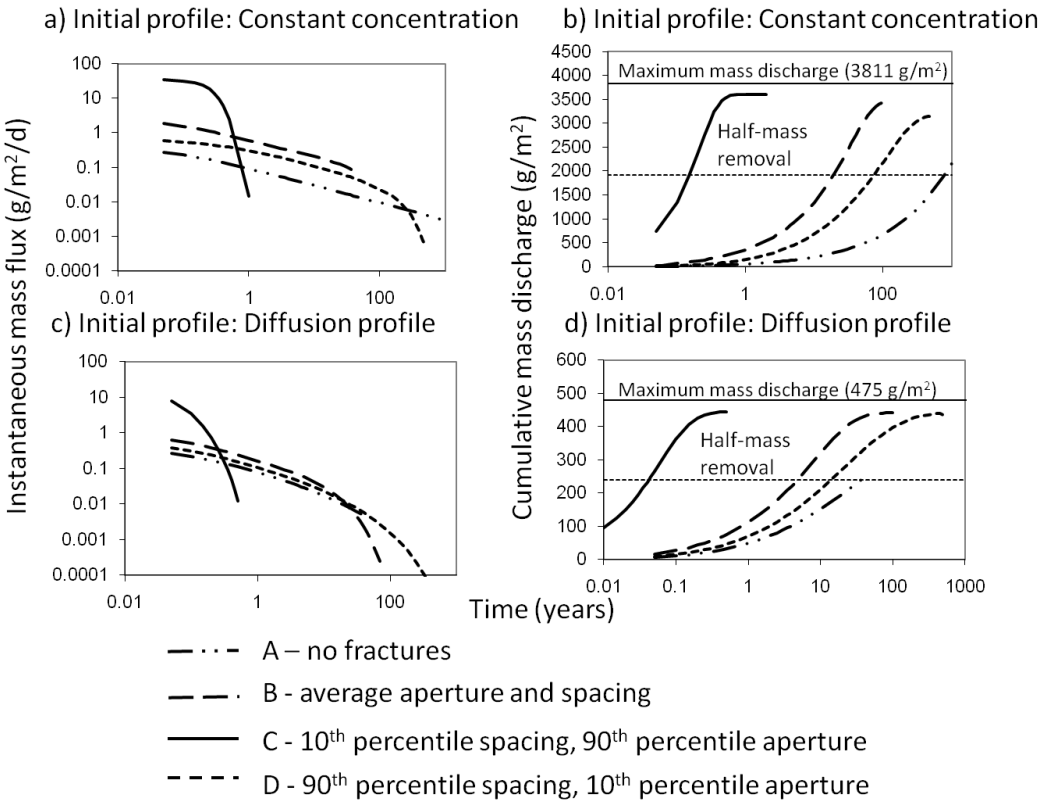

Figure 21 Simulation results with different initial concentration distributions, including; a) instantaneous flux from a constant concentration profile; b) cumulative discharge from a constant concentration profile; c) instantaneous flux from a diffusion profile, and d) cumulative discharge from a diffusion profile. Scenario A) diffusion only (no fractures), Scenario B) Set 1; 2b 17 mm, Sp 2.08 m, et 2; 2b 0.035 mm, Sp 0.63 m); scenario C) Set 1; 2b 49 mm, Sp 0.567 m, Set 2; 2b 0.1 mm, Sp 0.047 m), and scenario D) Set 1; 2b 5 mm, Sp 3.37 m, Set 2; 2b 0.01 mm, Sp 1.726 m)

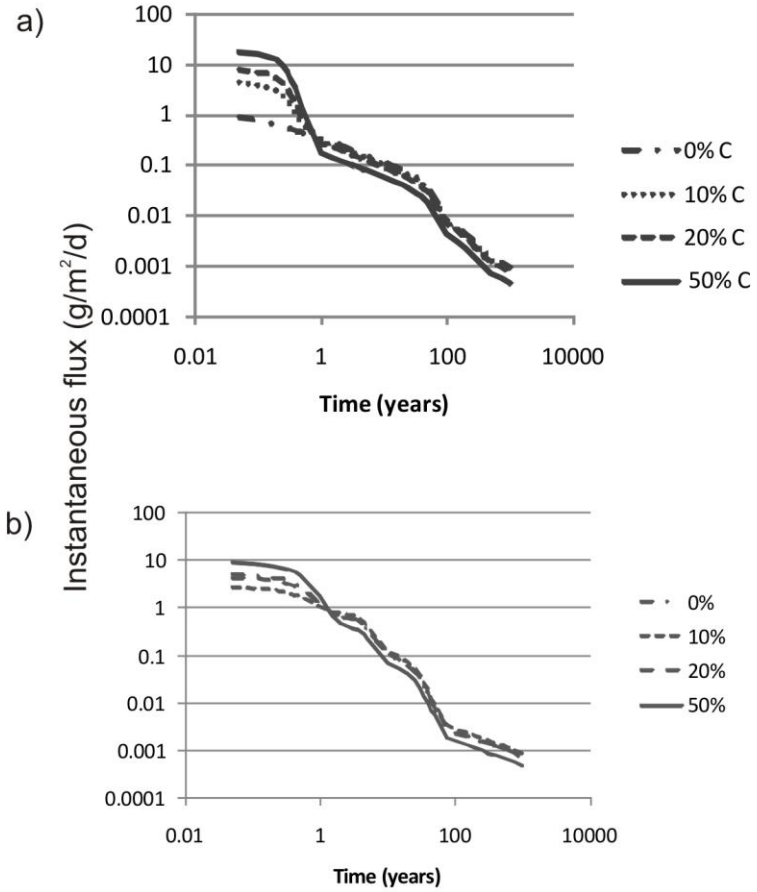

Figure 22 Instantaneous flux from mudstone fractured with differing proportions of fractures, namely: a) 0%, 10%, 20% and 50% of scenario C fractures and equal proportions of scenario A, B and D fractures and b) 0%, 10%, 20% and 50% of 0.1 mm. 0.1 m spaced fractures and equal proportions of 0.050 mm/0.1 m, 0.050 mm/0.5 m, no fractures. Initial contaminant profile: constant concentration with depth